Optimization of the Electron-Beam-Lithography Parameters for the Moth-Eye Effects of an Antireflection Matrix Structure

Chung-Feng Jeffrey Kuo, Hung-Min Tu, Te-Li Su

Department of Polymer Engineering, National Taiwan University of Science and Technology, Number 43, Section 4, Keelung Road, Taipei, 106, Taiwan, Republic of China

Received 1 March 2006; accepted 9 May 2006
DOI 10.1002/app.24827
Published online in Wiley InterScience (www.interscience.wiley.com).

ABSTRACT: In this study, we mainly used the characteristics of electron-beam lithography in measurement control and direct-write technology to improve the physical restrictions and production processes of optical lithography and other nanopattern production methods. We did this by using a silicon wafer as a substrate, coating a negative-tone photoresist, and using scattering and the reflection produced by the collision of an electron beam with the wafer lattice and the proximity effect of a secondary electron inside the electron-beam photoresist to produce an antireflection matrix structure with a moth-eye effect. In addition, we used the Taguchi quality method with an orthogonal array to plan the experiment and the signal-to-noise ratio to analyze the experimental data, and in the experimental process, we produced a full factorial equivalent experiment, using very few experiment repetitions and deriving optimum conditions. Also, we used back-propagation neural networks to fine-tune significant factors, allowing the production of the deepest process control parameters and thereby imparting to the antireflection matrix structure the best effect. © 2006 Wiley Periodicals, Inc. J Appl Polym Sci 102: 5303–5313, 2006

Key words: atomic force microscopy (AFM); lithography; nanotechnology

INTRODUCTION

On land, lepidopteran insects such as moths and silkworms have aligned bumps in their eyes to improve their ability to see at night, increasing their ability to absorb light rays at night. This phenomenon is called the moth-eye effect; researchers have found that this aligned bump structure can effectively reduce the reflection of light and at the same time increase the light absorption rate. We can use these characteristics to improve the performance of our optical devices, improving the efficiency and effectiveness of our usage of light. In everyday life, solar cells absorb sunlight and produce electricity; in times of increasing energy shortages around the globe, this may be a way of solving our lack of sufficient electricity sources. However, the current energy utilization efficiency of solar cells is only in the range of 30–40%, and thus they can be used only on low-power-consumption devices. By using the moth-eye effect, we will be able to improve the light absorption efficiency of solar cells. In addition, in current mainstream liquid-crystal displays, the light source must pass through multiple transmission media; in this way, a large amount of light is lost, and inefficient light utilization results. To obtain sufficient lighting and brightness, displays need very powerful backlights, which result in relatively high energy consumption. By the incorporation of antireflection structures into optical devices, the efficiency of light utilization can be improved significantly; this enhances optical characteristics of devices and reduces energy consumption.

Currently, the relative theoretical basis of antireflection structure research has been built on the manipulation of exterior surfaces and alignment methods. Raguin and Morris[1] studied the one-dimensional characteristics of antireflection structures, pointing out the antireflection effects of using the cross section of a triangular or sine wave structure. Grann et al.[2] studied two-dimensional antireflection structure optimization, allowing Fresnel reflection to be reduced by about 20 db. These examples all proved the effectiveness of antireflection methods. Walheim et al.[3] used a polymer thin-film coating material and then removed it with a special solvent, giving the surface a cratered texture and obtaining an antireflection effect. Although this process is easy and efficient, the craters that are produced are all different in size and shape, and this makes it hard to control the size and mea-

Correspondence to: C.-F. J. Kuo (jeff@tx.ntust.edu.tw).
Contract grant sponsor: National Science Council of the Republic of China; contract grant number: NSC 93-2216-E-011-019.

surement characteristics, so its antireflection effect is limited for satisfying different requirements to produce antireflection effects for different wavelengths of light. Jiang et al.[4] fabricated diffraction gratings on hybrid sol–gel glass, using holographic interference lithography. Therefore, the products had optical size measurement limitations; diffraction, affecting the size and measurement precision, resulted at shorter wavelengths. Motamedi et al.[5] used binary optical technology to obtain an antireflection structure, but the production process required the introduction of a mask, which added to the complexity of the process. Raguin and Morris[6] researched antireflection structures in the infrared spectral range, but they did not do any research on any other wavelength ranges.

In addition, to produce the moth-eye effect, we need to design the structural depth according to the specific incident wavelengths, so depth control is very important in the structure formation process. In the current production methods, we encounter problems concerning production-method size and measurement restrictions and the structural strength of the aspect ratio when longer or shorter wavelengths are involved. The development of electron-beam-lithography technology is a breakthrough technology for the production of nanodevices; its characteristic is direct writing, giving more flexibility to the production needs of devices of different sizes and measurements, and it does not need to produce exposure masks with optical lithography. Therefore, producing an antireflection structure with the moth-eye effect via electron-beam lithography can be a solution to the limitations of current production methods.

EXPERIMENTAL

Equipment and materials

We used the Raith 50 electron-beam-lithography system (made by Raith Co., Dortmund, Germany) with a photoresist for the product of the antireflection matrix structure. The Raith 50 standard is shown as Table I. The photoresist (NANOTM SU-8 2000) was a negative-tone photoresist made by MicroChem (Newton, Massachusetts). All the measurements and analyses of the morphological properties were carried out with a MultiMode NanoScope IIIa atomic force microscope from Digital Instruments (Buffalo, New York), and the tapping probes were produced by Silicon-MDT (Wilsonville, Oregon) in cooperation with MikroMasch (Wilsonville, Oregon).

TABLE I
Standards of the Electron-Beam-Lithography System

Filament type	LaB6
Acceleration voltage	200 eV to 30 keV
Probe current range	5 pA to 20 nA
Writing field size	Variable, 0.5–1000 μm
Exposure step size	Write field/65,536
Writing speed	4-MHz area mode, 2-ns resolution
Working distance	Variable, 2–12 mm
Beam resolution	4 nm at 30 keV
Sample handling	45×45 mm^2 travel range
Laser interferometer	2-nm resolution
Current stability	<1%/h

Methodology

Antireflection matrix structure

This article discusses the reflection and transmission of light through two different interfaces. The behavior of light can be categorized into refraction and reflection according to the interface's natural optical characteristics. The refracted light passes through the interface with a bending angle according to the interface characterization. Reflected light reflects at an angle perpendicular to the incident light and does not pass through the interface. Because under general conditions the behavior of propagating light is similar to electromagnetic behavior, quantizing the light from refraction and reflection and using Ampĕre's law and Faraday's law to discuss the effects of electromagnetic waves passing through an interface,[7] we have obtained an equation for the relationship between the reflection rate of normal incidence (R) and the interface:

$$R = \left(\frac{n_2 - n_1}{n_2 + n_1}\right)^2 \tag{1}$$

where n_1 and n_2 are the reflection coefficients of the two interfaces. Then, the transmission (T) is

$$T = 1 - R = \frac{4n_2n_1}{(n_2 + n_1)^2} \tag{2}$$

At $n_1 = n_2 = 0$ [which means that the light is propagating through an area with no transmission medium (vacuum)], $R = 0$, and $T = 0$, with eq. (2) as our basis, we can obtain the relationship between the light's reflection rate and transmission: reducing the reflection increases the opportunity for light to pass through the interface.

The moth-eye effect was first discovered by Bernhard;[8] he observed the cornea surface of a moth's eye under an electron microscope and found an approximately 200-nm aligned lumped structure, as shown in Figure 1. This means that this structural characteristic can change the reflection coefficient of light passing through air and the cornea. This continuously changing reflection coefficient can effectively reduce the production of reflected light, and the reflection coefficient (n) is[9]

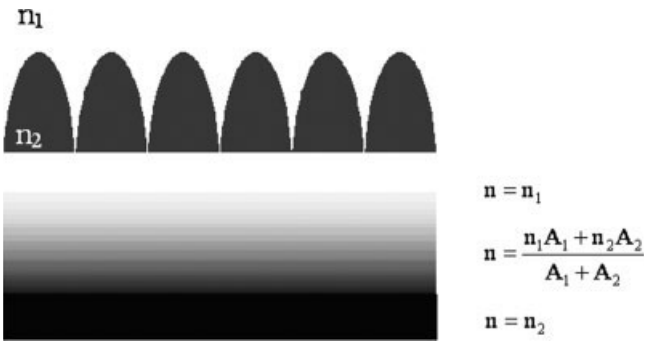

Figure 1 Cornea structure of a moth's eye.

$$n = \frac{n_1 A_1 - n_2 A_2}{A_1 + A_2} \tag{3}$$

where A_1 and A_2 are the projected areas on media n_1 and n_2, respectively.

In research on the reflection coefficient, Clapham and Hutley[10] extended the argument that the reflection coefficient of the continually changing medium can effectively reduce the total amount of reflected energy for the overall structure, and they claimed that this results from specific changes in the incident wavelength (λ) and the structural depth (d) of the material. Because of the difference in the reflection coefficients at each different depth, the incident light waves interfere with one another destructively, thereby reducing the overall reflection rate. When the ratio of d to λ is 0.4 or a multiple of 0.4, the reflection coefficient will be at a minimum. Through Hadobás et al.'s[11] experiment, it has been proven that when the incident light source is in the range of 200 nm $< \lambda <$ 3000 nm, and the range of d is 35–190 nm; reflection coefficient n undergoes continuous and periodical change according to the change in the depth. As shown in Figure 2, by observing the relationship between the d/λ ratio and reflection rate R under a 1000-nm light source, we find that R is close to zero when the d/λ ratio is a multiple of 0.4. This means that an optimal antireflection effect is obtained when the ratio of d to λ is 0.4 or any multiple of 0.4.

Proximity effect

In electron-beam-lithography production technology, the production of the proximity effect occurs when the structural pattern is very similar and the close and neighboring pattern is affected by the energy from the electron scattering and undergoes exposure in the exposure process. This results in differences in the sizes and measurements of the actually obtained pattern and the designed pattern; especially when the designed patterns are really dense, the actually obtained patterns are larger than those that were originally designed, and the pattern resolution and precision are affected the most. This phenomenon results from secondary electron scattering back to the photoresist layer caused by electrons bumping into one another after the emitting electron is in the photoresist and the electron beam reaches the substrate, as shown in Figure 3.[12] With poly(methyl methacrylate) with a high tension exposed to 10- or 20-kV electron beams, with Si as its substrate, the figure shows the condition of the scattering of the electrons. The vertical axis and horizontal axis are the distances along the x and z directions, respectively; the higher the high tension is, the deeper the electron-beam exposure is, but also the severer the relative electron scattering is, and the greater the proximity effect is. In addition, different electron scattering conditions appear with different photoresists and different substrates.

To improve the proximity effect, exposure simulation software used to analyze and change the exposure parameters is usually applied, or methods such as the reservation of extra space in the pattern design stage can also be employed. Kruger et al.[13] studied the technology of a multilayer photoresist, but this method cannot totally eliminate the effect of the backscattering electrons and is unable to provide enough resolution for submicrometer patterns. The equalization of the background dose (GHOST), intro-

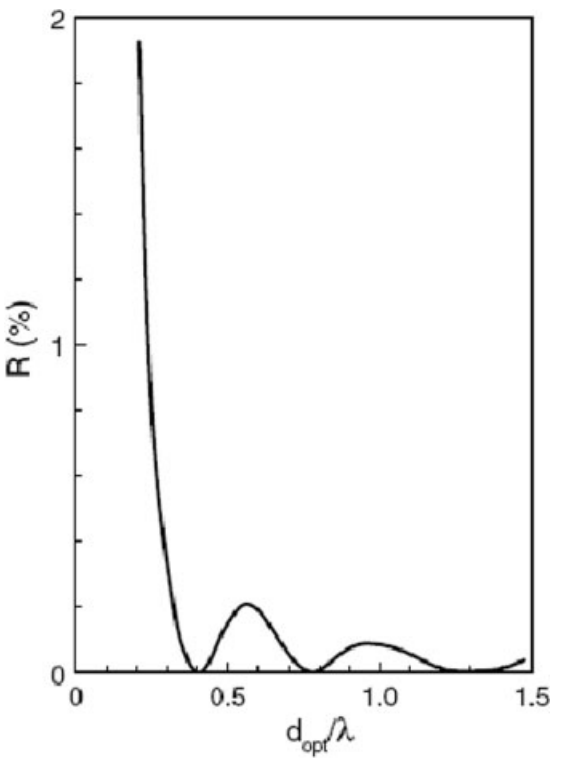

Figure 2 Relation between the reflection rate [R (%)] and structural depth/wavelength ratio (d_{opt}/λ).

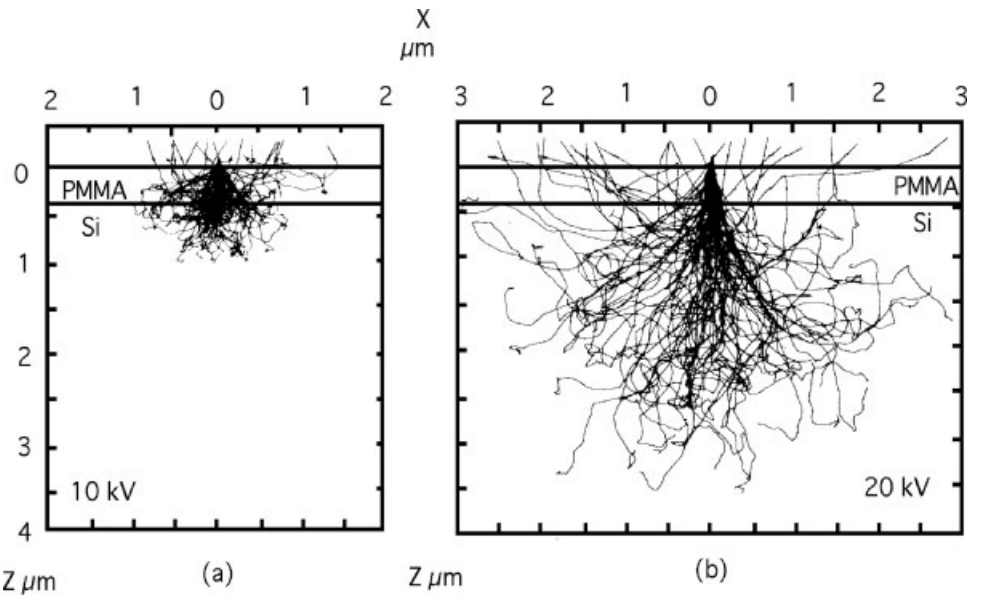

Figure 3 Electron scattering conditions under the proximity effect.

duced by Owen and Rissman,[14] uses a backscattering-electron, exposure-strength, nonfocused electron beam to draw the unexposed area in advance. Its disadvantage is that it reduces the contrast of the photoresist and might produce flaws in the photoresist. The dose-modulation technique introduced by Parikh[15] cuts the pattern into several regions and exposes it to different intensities according to its energy distribution. As with the shape-correction method of Jacob et al.,[16] it is possible to modify the pattern in the data processing process, such as shrinking the size of a pattern in which the electron scattering is more severe, but the modification of the patterns and the dose-modulation technique take a long time for computers to simulate and calculate. All these methods improve the proximity effect during the production of nanopatterns.

Because the changes made by the proximity effect to the exposure characteristics of the nanopatterns during their production and formation coincidentally are exactly the changes needed to obtain the moth-eye structure, this study uses the proximity effect to produce indirect exposure to close and neighboring patterns, thereby producing antireflection structures. The equation for the proximity effect is[17]

$$f(r) = \frac{1}{1+\eta}\left[\frac{1}{\pi\alpha^2}\exp\left(-\frac{r^2}{\alpha^2}\right) + \frac{\eta}{\pi\beta^2}\exp\left(-\frac{r^2}{\beta^2}\right)\right] \quad (4)$$

where f is the exposure energy, α is the forward scattering coefficient, β is the backscattering coefficient, η is the ratio of backscattering exposure energy to forward scattering exposure energy, and r is the distance from the center of the electron beam. From eq. (4), we know that the exposure energy and distance are a Gaussian function combination. Thus, this study uses the generation of the proximity effect, altering the distance between backscattering and forward scattering or neighboring patterns by modifying the exposure parameters and thereby obtaining the designed antireflection matrix structure.

Taguchi quality method

The performance of an antireflection matrix structure is related to the control factors, but the interaction between the factor levels needed to be thoroughly explored. To investigate the relationship between the electron-beam-lithography parameters and their values, the experiment had to be planned and executed, and the trial results were analyzed with statistical methods. The concepts of the Taguchi quality method are exploited in an electron-beam-lithography system, which is not sensitive to the environment, through the parameter design to simplify the variable influence and minimize the variance of quality or process and to reach a robust design.[18–20] The signal-to-noise (SN) ratio of the quality characteristic, the depth of the antireflection matrix structure, belongs to the larger-is-best situation and can be calculated with the following equation

$$\eta = -10\log\left(\sum(1/y^2)/n\right) \quad (5)$$

where y is the value of the experimental observations and n is the number of experiments.

After conducting the experiment, we had to calculate the main effects on each factor because this could indicate the influence of each factor on the quality characteristic. The calculations can be expressed in terms of the following equations:

$$\bar{f}_i = \frac{1}{m}\sum_{j=1}^{m} \eta_j \tag{6}$$

$$\Delta f = \max(\bar{f}_1, \bar{f}_2, \ldots, \bar{f}_d) - \min(\bar{f}_1, \bar{f}_2, \ldots, \bar{f}_d) \tag{7}$$

where $\bar{f}_i$ is the mean S/N ratio for the ith level of factor f, m is the number of the ith level of each factor, η_j is the jth SN ratio of the ith level, and d is the number of the level of each factor.

To estimate effectively the observation values of the factor levels and their results, the confidence interval (CI) for a confirmation experiment has to be calculated and can be executed as follows:

$$\mathrm{CI} = \sqrt{F_{\alpha;1,\nu 2} \times V_e \times \left(\frac{1}{n_{eff}} + \frac{1}{r}\right)} \tag{8}$$

where $F_{\alpha;1,\nu 2}$ is the tabulated F ratio, α is the risk (confidence level = 1 − α), $\nu 2$ is the number of degrees of freedom for the numerator associated with the pooled error variance (V_e), and r is the sample size.

When $\hat{\eta}$ is the SN ratio estimation with the optimum factor levels, the processing parameter estimated is represented by μ, and their expressions are as follows:

$$\hat{\eta} = T + \sum_{i=1}^{q} \bar{f}_i - T \tag{9}$$

q is the number of significant processing parameters, T is the total average of the SN ratios in the experiment, and $\bar{f}_i$ is the mean response value of the ith level of the significant processing parameters:

$$\hat{\eta} - \mathrm{CI} \le \mu \le \hat{\eta} + \mathrm{CI} \tag{10}$$

Back-propagation neural network (BPNN)

The basic principle of the BPNN model is to use the concept of the gradient steepest descent method to minimize the energy function:

$$E = \frac{1}{2}\sum_{k} (Y_{dk} - Y_k)^2 \tag{11}$$

where Y_{dk} is the target output value of the output layer and Y_k is the ratiocinated value of the output layer. In this research, the target output value is the SN ratio of the depth of the antireflection matrix structure. The learning parameters—the input layer of 4, the hidden layer of 3, the output layer of 1, the learning cycle of 10,000, the learning rate of 0.5, and the momentum factor of 0.5—were set in our BPNN model. Its learning process usually gives one training datum once until all training data sets are completed. The training data set can be iterated many times in a network (even a 1000 times depending on the complexity of a problem) until the learning effect of the network is converged. A BPNN is a supervised learning network. It is adopted for diagnosis and prediction.[21–23] The predictive model in this study was constructed with a BPNN, as shown in Figure 4. During the entire process of network learning, the weight change of an output layer to a hidden layer is calculated as follows:

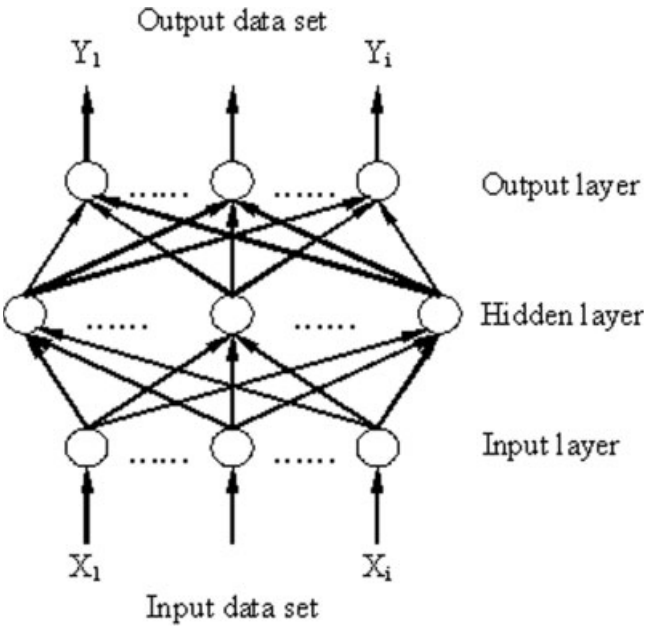

Figure 4 Schematic diagram of the three-layer BPNN architecture.

$$\Delta W_{jk} = -\eta \frac{\partial E}{\partial W_{jk}} = -\eta \frac{\partial E}{\partial Y_k}\frac{\partial Y_k}{\partial net_k}\frac{\partial net_k}{\partial W_{jk}} \tag{12}$$

$$\frac{\partial E}{\partial Y_k} = \frac{\partial}{\partial Y_k}\left(\frac{1}{2}\sum_{k}(Y_{dk} - Y_k)^2\right) = -(Y_{dk} - Y_k) \tag{13}$$

$$\frac{\partial Y_k}{\partial net_k} = f_0'(net_k) \tag{14}$$

$$\frac{\partial net_k}{\partial W_{jk}} = \frac{\partial}{\partial W_{jk}}\left(\sum_{k} H_j W_{jk}\right) = H_j \tag{15}$$

$$\Delta W_{jk} = -\eta[-(Y_{dk} - Y_k)]\, f_0'(net_k) H_j = -\eta \delta_k H_j \tag{16}$$

$$\delta_k = -(Y_{dk} - Y_k) f_0'(net_k) \tag{17}$$

$$\Delta \theta_k = -\eta \delta_k \tag{18}$$

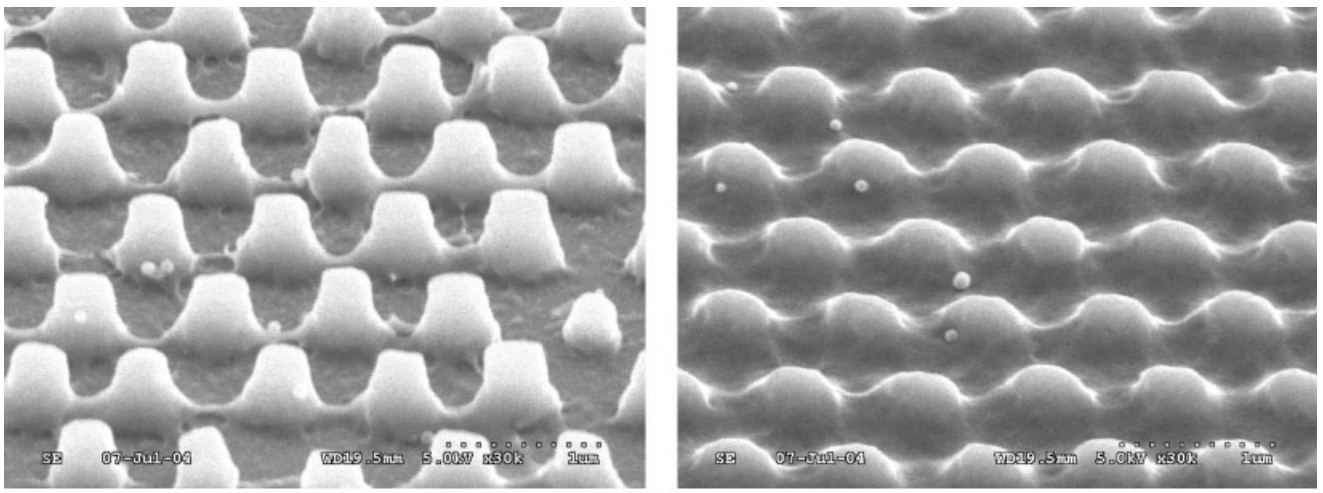

(a) (b)

Figure 5 Effects of different electron beam voltages on the exposure.

The weight change of the hidden layer to the input layer is calculated as follows:

$$\Delta W_{ij} = -\eta \delta_j X_i \tag{19}$$

$$\begin{aligned}\delta_j &= \sum_k \frac{\partial E}{\partial H_j}\frac{\partial H_j}{\partial net_j} \\ &= \sum_k \frac{\partial E}{\partial Y_k}\frac{\partial Y_k}{\partial net_j}\frac{\partial net_j}{\partial H_j}\frac{\partial H_j}{\partial net_j} \\ &\times \sum_k [-(Y_{dk} - Y_k)]\, f_0(net_k)\frac{\partial}{\partial H_j} \times \left(\sum_j H_j W_{jk}\right)\frac{\partial H_j}{\partial net_j} \\ &= -\sum_k (Y_{dk} - Y_k) f_0(net_k) W_{jk} f'_H(net_j) \\ &= \sum_k (\delta_k W_{jk}) f'_H(net_j)\end{aligned} \tag{20}$$

$$\Delta W_{ij} = -\eta \sum_k (\delta_k W_{jk}) f'_H(net_j) X_i = -\eta \delta_j X_i \tag{21}$$

$$\Delta \theta_j = -\eta \delta_j \tag{22}$$

where η is the learning rate; $\Delta\theta_k$ and $\Delta\theta_j$ are the threshold values of the output layer to the hidden layer; and ΔW_{ij} and ΔW_{jk} are the weighted value revising functions between the input layer and hidden layer and between the hidden layer and output layer, respectively. During the process of network learning, the formula for revising the weighted value is

$$\Delta W^{n+1} = \eta \delta X + \alpha \Delta W^n \tag{23}$$

where ΔW^{n+1} is the $(n + 1)$th weight change, ΔW^n is the nth weight change, and α is the momentum

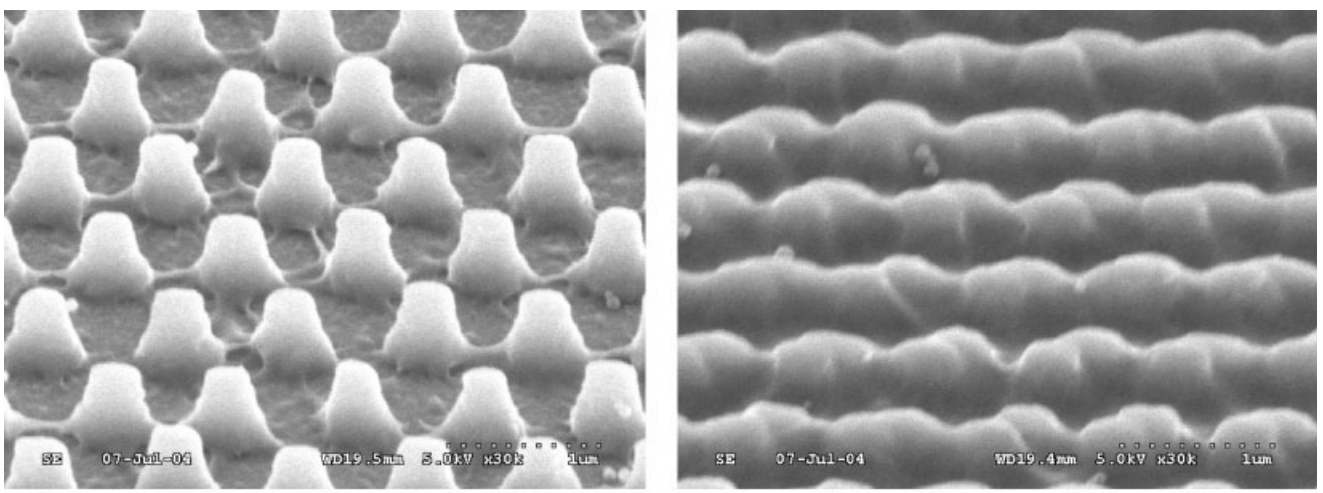

(a) (b)

Figure 6 Effects of different electron-beam measurements on the exposure.

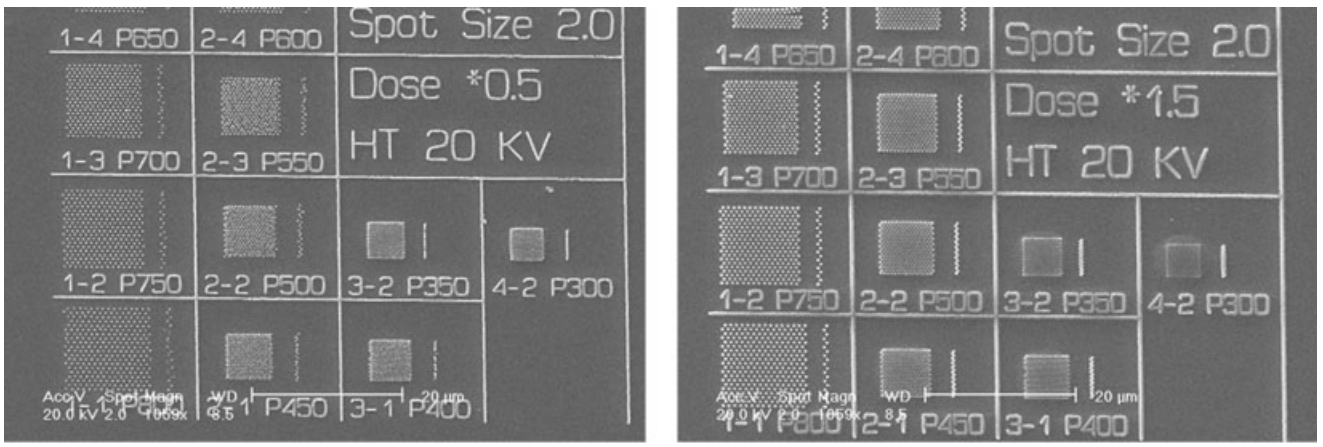

Figure 7 Effects of different exposure dosages on the structure.

factor. This network computation can be divided into two portions: the prior teaching computation and the reverse adjusting the weighted value. During the entire computation process of the neural network, the exchange function can be used to control the kind of output unit. In this research, we have used a nonlinear curving function:

$$f(x) = \frac{1}{1 + e^{-x}} \tag{24}$$

The root-mean-square error (RMSE) is usually calculated to reflect the degree to which learning has taken place in the network, and the equation for the RMSE value is calculated as follows:

$$\text{RMSE} = \sqrt{\frac{\sum_p^M \sum_j^N \left(T_j^p - Y_j^p\right)^2}{M \times N}} \tag{25}$$

where T_j^P is the target value for output unit j after presentation of signal p, Y_j^p is the output value produced by output unit j after the presentation of signal p, M is the number of signals in the training set, and N is the number of units in the output layer.

This measure reflects how close the network is to getting the correct answers. As the network learns, its RMSE decreases. Generally, an RMSE value below 0.1 indicates that a network has learned its training set.

RESULTS AND DISCUSSION

The first step in this experiment is to evaluate and eliminate those parameters of the electron-beam-lithography control parameters that affect exposure or that cannot be easily controlled. Through a series of experiments, we set the following four control factors: high tension, electron-beam measurements, exposure dosage, and pitch. Then, we set the depth of the dot pattern after exposure as the quality characteristic. From the Taguchi method, we obtained the equality characteristic of the larger-the-better, that is, the deeper the better for antireflection matrix structure. We also explored the effect that the four control factors have on the depth in the hope of being able to set appropriate levels.

High tension

Electron-beam lithography excites electrons by increasing the voltage to a filament and exposes the photoresist by focusing the collected electron beam onto the photoresist. As shown in Figure 5, the voltage level in part a is 20 kV, and the voltage level in part b is 10 kV. When a high voltage is applied to

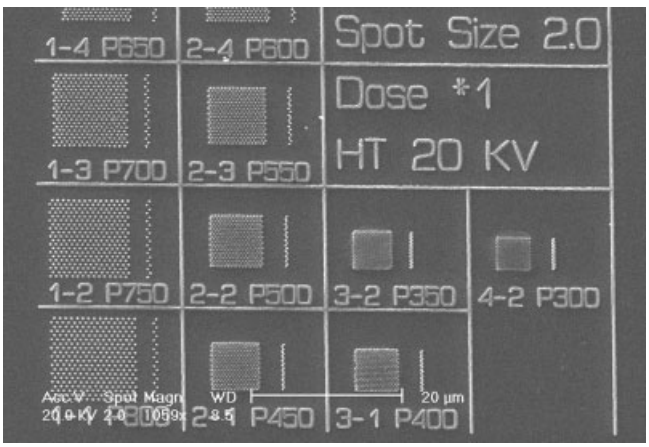

Figure 8 Effects of different pitch distances on the exposure.

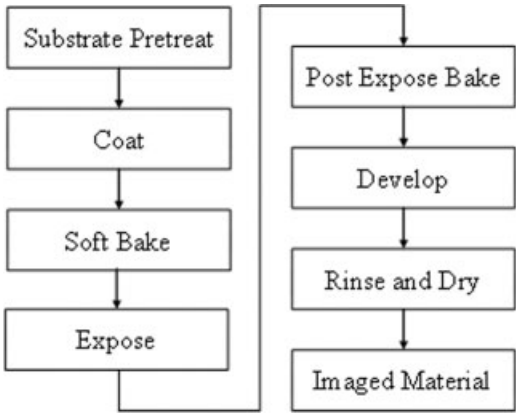

Figure 9 Procedure flow for producing an antireflection matrix structure.

the filament, the generated electron beam is more centered and focused, and the exposure energy is also centered. At a lower voltage, the energy for the generation of the electron beam is lower and less centered and focused. The more centered the electron beam is, the higher the control precision is that we have over the size measurements. This can reduce the proximity effect produced, but increasing the value of the high tension also increases the chance of producing irregular patterns.

Spot size

As shown in Figure 6, the measurement of the electron beam in part a is 1.6, and that in part b is 2.2. Under the same high tension (high tension = 20 kV), dosage (dose factor = 1), and pattern pitch (pitch = 600 nm), we observe the effect that the change in the electron-beam measurements has on the structure's size measurements: larger electron beams result in enlarged structures. Because the figures show equivalent pitches, the electron beam that measures 2.2 results in proximity effects appearing between neighboring point structures. The structures overlap each other and affect the depth of the overall array structure.

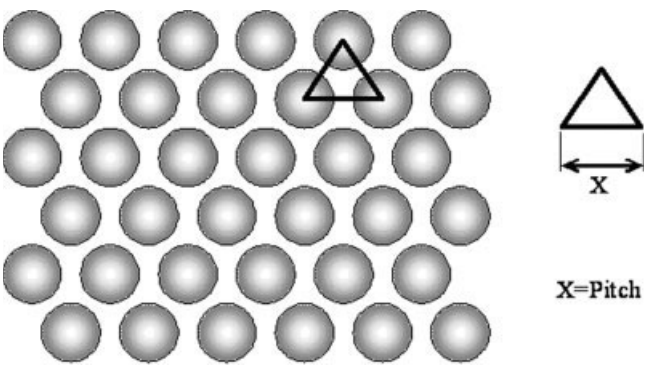

Figure 10 Design diagram for an antireflection matrix structure.

TABLE II
Four Control Factors and Their Levels

	Level		
Control factor	1	2	3
A. High tension (kV)	20	15	10
B. Spot size (μm)	2.0	1.6	1.2
C. Dose (fAs)[a]	1	2	3
D. Pitch (nm)[a]	1	2	3

[a] The numbers are explained in Table III.

Dose

As shown in Figure 7, the exposure dosage in part a is 0.5 times the standard exposure dosage, and the exposure dosage in part b is 1.5 times the standard exposure dosage. Under the same parameter settings, in the figure obtained after exposure and development, because 0.5 times the standard dosage is a relatively small dosage, in wider pattern pitches, as shown in 1–2 P750 (pitch = 750 nm), the patterns are farther apart, and the proximity effect is smaller; therefore, the exposure energy is smaller.

Pitch

As shown in Figure 8, with the pattern pitch gradually becoming smaller, each dot pattern is affected more and more by its neighboring patterns. Originally, we could easily make out the type of dot pattern, but when the pitch gradually becomes smaller (the pitch in the figure shrinks from 800 to 300 nm), the patterns start to overlap; this affects the depth of the pattern and makes it shallower, finally making it impossible to make out the alignment condition of the dot matrix structure.

The production process of antireflection matrix structures is shown in Figure 9. The design diagram of an antireflection matrix structure is shown in Figure 10.

TABLE III
Dose/Pitch Levels

	Dose/pitch		
No.[a]	Level 1	Level 2	Level 3
1	0.5/350	0.7/450	0.9/550
2	0.4/450	0.6/550	0.8/650
3	0.3/600	0.5/700	0.7/800

[a] The numbers refer to rows C and D in Table II.

TABLE IV
Orthogonal Array with the Averages and SN Ratios

	L_9[a]				Experimental result	
Experiment	A	B	C	D	$\bar{y}$	η (dB)
1	20	2.0	0.5	350	344.667	50.739
2	20	1.6	0.7	450	374.000	51.456
3	20	1.2	0.9	550	401.000	52.051
4	15	2.0	0.6	650	402.333	52.087
5	15	1.6	0.8	450	249.000	47.813
6	15	1.2	0.4	550	340.333	50.629
7	10	2.0	0.7	700	430.667	52.681
8	10	1.6	0.3	800	385.000	51.594
9	10	1.2	0.5	600	416.000	52.382

[a] The letters refer to rows A–D in Table II.
$\bar{y}$ is the average value of the experimental observations.

We chose the $L_9(3^4)$ orthogonal array and proceeded with nine experiments. The levels of the four control factors are shown in Table II, in which the levels of the dosage and pitch are set to a sliding level to reduce interactions because of concerns of interactions with high tension; their level values are shown in Table III.

After completing nine experiments according to orthogonal array, using an atomic force microscope to measure the structural matrix's depth, we collected three different measurement values from the measurement area. Then, we calculated the SN ratios for each respective experiment and recorded the results in Table IV. After obtaining the SN ratio for each experiment, we also obtained the response table and response graph through main-effect analysis; these are shown in Table V and Figure 11.

From the response table and response graph, we have found that the preliminary optimized combination of the control factor levels is A3, B1, C2, and D3, that is, a high tension of 10 kV, a spot size of 2.0 μm, a dose of 0.6 fAs, and a pitch of 800 nm. According to the results of three confirmation experiments, its SN ratio is 51.697dB, which falls inside the corresponding trusted region (49.865–52.207); this means that the factorial result has reproducibility, which means that this is an accountable experiment.

TABLE V
Responses of Main Effects with the SN Ratios

	Level				
Control factor[a]	1	2	3	Main effect	Rank
A	51.415	50.176	52.219	2.042	1
B	51.836	50.288	51.687	1.548	3
C	50.988	51.975	50.848	1.127	4
D	50.311	51.589	51.911	1.599	2

[a] The letters refer to rows A–D in Table II.

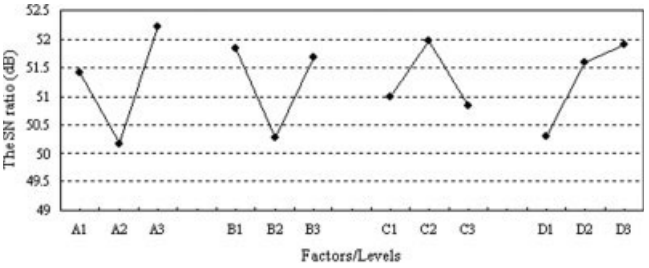

Figure 11 Response graph of the SN ratio.

To further understand the degree of influence that the control factors have on the depth, we analyzed the quality characteristics using an analysis of variance (ANOVA); the results are as shown in Table VI. From the ANOVA table, we see that the high tension and spot size are noticeable control factors.

We used a BPNN as a tool to help us adjust the control parameters to an optimized setting. There are four input neurons—the high tension, spot size, dose, and pitch—and one output neuron—the SN value of the depth of the antireflection matrix structure. We finished 50 experiments by trial and error for the learning parameter of the BPNN. The better convergence result is reached with an RMSE value of 0.000311, whereas the number of hidden neurons is 3, the learning rate is 0.5, and the momentum factor is 0.5. The RMSE diagram of the neural network is shown in Figure 12. After setting up the forecast model for the system using the BPNN, we directed our attention to the optimal control parameter combination obtained through the Taguchi method and further fine-tuned the parameter with the most noticeable influence in the hope of finding an antireflection structural depth that is even closer to the ideal. In the ANOVA table, we observed that the high tension and spot size are the control factors with the most noticeable effects. Therefore, we used our trained network as a helping tool to fine-tune the high tension and spot size five times. We added four random values near the optimum parameter level for the high tension and spot size, and this resulted in 8, 9, 10, 11, and 12 kV for the high

TABLE VI
ANOVA

Source[a]	Degree of freedom	Sum of squares	Variance	*F*
A	2	38,248.96	19,124.48	46.3229
B	2	21,897.85	10,948.93	26.5202
C	2	8,889.19	4,444.59	10.7656
D	2	17,965.41	8,982.70	21.7577
Error	18	7431.33	412.85	—
Total	26	94,432.74		

[a] The letters refer to rows A–D in Table II.

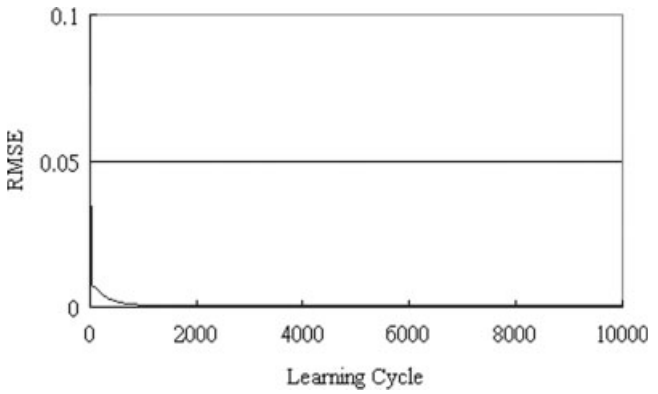

Figure 12 RMSE diagram of the neural network.

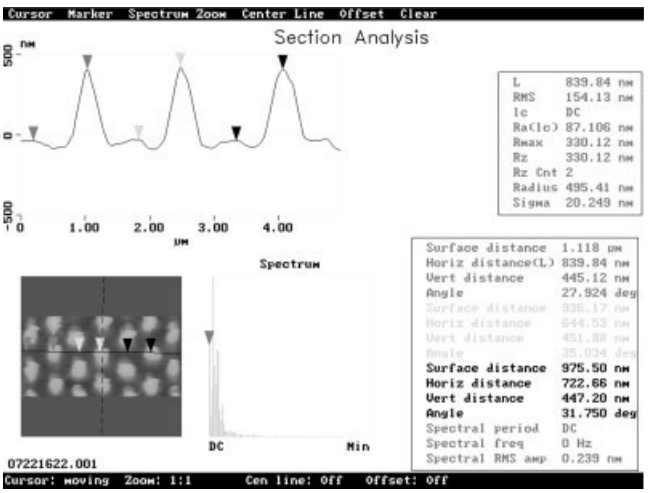

Figure 13 Diagram of the confirmation experiment.

tension and 1.8, 1.9, 2.0, 2.1, and 2.2 μm for the spot size. Then, we forecast them using the network.

We can observe in Table VII that no. 4 has the largest SN ratio value and therefore is the optimized electron-beam-lithography (EBL) control parameter combination for this study. Finally, through a confirmation experiment, we obtained the results of the optimized EBL parameter combination measured with atomic force microscopy, as shown in Figure 13. Table VIII compares the results of the optimum condition obtained from the Taguchi method and modified Taguchi method by the BPNN; the mean depth values are 401.986 and 447.667 nm, respectively. Obviously, the results obtained after further fine tuning with the BPNN are better.

CONCLUSIONS

We have successfully produced a moth-eye-effect antireflection matrix structure using electron-beam lithography and also combined the Taguchi method with a BPNN to forecast an optimized control parameter combination. Because electron-beam-lithography technology has even better measurement precision and an even simpler production process than optical lithography, electron-beam lithography can be used to directly produce a designed pattern, and this is a big advantage in terms of pattern production in comparison with optical lithography, for which a mask must first be created. By controlling the electron-beam-lithography system parameters, we have even more flexible reactions to pattern changes, allowing the production of even more complex or even smaller pattern structures. However, electron-beam lithography has a limited capacity for the fabrication of a large area of an antireflective layer because of the time-consuming sequential nature of the exposure method. Through this study, we have obtained the optimal process parameters for the production of an antireflection matrix structure, and we can use this structure to create a mold and use repeated nanoimprinting to pattern a large area of an antireflective layer. Moreover, in the future we may apply these techniques to give this antireflection structure an even broader range of applications for everyday life, and finally we may be able to use antireflection structures to give us an advantage in energy exploitation, reducing the amount of wasted energy.

TABLE VII
Fine Tuning of the BPNN Processing Parameters

	Condition[a]				
Control factor	1	2	3	4	5
High tension (kV)	8	9	10	11	12
Spot size (μm)	1.8	1.9	2.0	2.1	2.2
Dose (fAs)	0.6	0.6	0.6	0.6	0.6
Pitch (nm)	800	800	800	800	800
Predicted SN ratio (dB)	51.37	51.78	52.54	53.02	52.36

[a] Condition obtained from Table V and Figure 11 for fine tuning the processing parameters.

TABLE VIII
Comparison of Two Processing Conditions

	Condition	
Control factor	1[a]	2[b]
High tension (kV)	10	11
Spot size (μm)	2.0	2.1
Dose (fAs)	0.6	0.6
Pitch (nm)	800	800
Mean depth (nm)	401.986	447.667

[a] Optimum condition by the Taguchi method.
[b] Optimum condition based on the modified Taguchi method by BPNN.

This research was supported by the Instrument Technology Research Center of Taiwan. The authors thank Y. C. Hu and H. L. Yin for their assistance with this study.

References

1. Raguin, D. H.; Morris, G. M. Appl Opt 1993, 32, 2582.
2. Grann, E. B.; Moharam, M. G.; Pommet, D. A. Opt Soc Am 1995, 12, 333.
3. Walheim, S.; Schäffer, E.; Jürgen, M.; Steiner, U. Science 1999, 283, 520.
4. Jiang, H. J.; Yuan, X.-C.; Zhou, Y.; Chan, Y. C.; Lam, Y. L. Opt Commun 2000, 185, 19.
5. Motamedi, M. E.; Southwell, W. H.; Gunning, W. J. Appl Opt 1992, 31, 4371.
6. Raguin, D. H.; Morris, G. M. Appl Opt 1993, 32, 1154.
7. Wolfson, R.; Pasachoff, J. M. Physics with Modern Physics for Scientists and Engineers; HarperCollins: New York, 1995; Chapter 35, p 896.
8. Bernhard, C. G. Endeavour 1967, 26, 79.
9. Johnsen, S. Biol Bull 2001, 201, 301.
10. Clapham, P. B.; Hutley, M. C. Nature 1973, 244, 281.
11. Hadobás, K.; Kirsch, S.; Carl, A.; Acet, M.; Wassermann, E. F. Nanotechnology 2000, 11, 161.
12. Kyser, D. F.; Viswanathan, N. S. J Vac Sci Technol 1975, 12, 1305.
13. Kruger, J. B.; Rissman, P.; Chang, M. S. J Vac Sci Technol 1981, 19, 1320.
14. Owen, G.; Rissman, P. J Appl Phys 1983, 54, 3573.
15. Parikh, M. J Vac Sci Technol 1978, 15, 931.
16. Jacob, J.; Lee, S.; McMillan, J.; MacDonald, N. J Vac Sci Technol B 1992, 10, 3077.
17. Chang, T. H. P. J Vac Sci Technol 1975, 12, 1271.
18. Deng, C. S.; Chin, J. H. Int J Adv Manuf Technol 2005, 25, 420.
19. Saglam, H.; Unsacar, F.; Yaldiz, S. Int J Prod Res 2005, 43, 2309.
20. Lee, B. H.; Abdullah, J.; Khan, Z. A. J Mater Process Technol 2005, 169, 54.
21. Matlaya, R.; M'Sahli, F. Int J Adv Manuf Technol 2005, 26, 161.
22. Ding, L.; Yue, Y.; Ahmet, K.; Jackson, M.; Parkin, R. Int J Prod Res 2005, 43, 3247.
23. Sanjay, C.; Neema, M. L.; Chin, C. W. J Mater Process Technol 2005, 170, 494.